Journal of Membrane Science 620 (2021) 118892

Contents lists available at ScienceDirect

Journal of Membrane Science

journal homepage: http://www.elsevier.com/locate/memsci

# Comparison of the effects of edge functionalized graphene oxide membranes on monovalent cation selectivity

Ruosang Qiu [a], Jie Xiao [b], Xiao Dong Chen [b], Cordelia Selomulya [a,c], Xiwang Zhang [a], Meng Wai Woo [a,d,*]

[a] Department of Chemical Engineering, Monash University, Clayton, Victoria, 3800, Australia
[b] China-Australia Joint Research Centre in Future Dairy Manufacturing, School of Chemical and Environmental Engineering, College of Chemistry, Chemical Engineering and Materials Science, Soochow University, Suzhou, Jiangsu Province, 215123, PR China
[c] School of Chemical Engineering, UNSW, Sydney, NSW, 2052, Australia
[d] Department of Chemical and Materials Engineering, The University of Auckland, Grafton, Auckland, 1023, New Zealand

ARTICLE INFO

*Keywords:*
Edge functionalized graphene oxide membrane
Monovalent cation selectivity
Ion dehydration
Ion hydration shell compression
Interaction between hydrated ions

ABSTRACT

Layer-by-layer graphene oxide (GO) membrane in principle has great potential in separating $Li^+$ from monovalent cations, which is achieved by their functionalized interlayer entrance. The edge effects on different monovalent ions, however, are not fully understood. Therefore, molecular dynamics simulations were utilized in this study to separately elucidate the filtration effects of three typical edge functional groups, which were carboxyl (COOH), hydroxyl (OH), and hydrogen (H), on the LiCl, NaCl, and KCl solutions. The results revealed that the water permeance was dominantly influenced by the steric size of edge functional groups. It could also be affected by the ions blocked at the entrance. The drastic dehydration of the hydrated $Na^+$ and $K^+$ caused by the OH edge required more energy that led to higher ion rejection. The compressed-dehydrated hydration shell, which was tuned by the edge functional groups, introduced repulsion from $Na^+$ and attraction from $Li^+$ on $Cl^-$ when they were 3–5 Å away from each other. It would be strategic to use all three edge functional groups to retain NaCl in the retentate stream while allowing selective permeance of LiCl and the OH edge could additionally retain KCl.

## 1. Introduction

The demand for lithium-ion batteries is growing rapidly because of the development of wearable equipment. Over sixty percent of lithium, the most important component for lithium battery, is stored in naturally available brine sources [1]. Since they are mixed with other ions in solution, especially $Na^+$ and $K^+$, the separation and collection of $Li^+$ is difficult [2,3]. Therefore, any potential improvement in the separation efficiency and selectivity of $Li^+$ from monovalent ions will directly translate to reducing the production cost of the lithium-ion battery.

Conventional methods used for separating $Li^+$ out from brines include precipitation, ion exchange, and liquid-liquid extraction. Those methods need extra reactants and cannot be processed continuously [3]. As one of the most effective and environment-friendly separation methods, membrane separation technology has been reported as a suitable process for $Li^+$ recovery from brines [4]. Most of the reported experiment trials on the ion separation hitherto only focused on the use of conventional polymeric membranes. Their rejection ratio of monovalent ions, however, usually is higher than 85% and necessary to be further decreased for industrial processing [5,6]. Compared to the irregular channels of conventional polymeric membranes, uniform channels of the layer-by-layer two-dimensional (2D) membrane theoretically could achieve better ion selectivity with higher separation efficiency [7]. Graphene oxide (GO) membrane is a type of 2D membrane that could be easily synthesized and utilized [8,9]. It has good chemical and mechanical stabilities, which make it possible for a wide variety of industrial applications [10]. The narrow interlayer entrance of the GO membrane, which consisted of functionalized edge and graphite surface, was reported as the key feature in this 2D membrane that dominantly contributes to the ion rejection. This functionalized entrance in cooperation with a low friction interlayer channel can hypothetically attain good monovalent ion separation performance [9–11]. Through entrance edge functionalization, which is nanosheet edge functionalization, the GO membrane selectivity can be adjusted corresponding to the

* Corresponding author. Department of Chemical and Materials Engineering, The University of Auckland, Grafton, Auckland, 1023, New Zealand.
*E-mail address:* meng.woo@monash.edu (M.W. Woo).

https://doi.org/10.1016/j.memsci.2020.118892
Received 9 August 2020; Received in revised form 1 November 2020; Accepted 3 November 2020
Available online 27 November 2020

characteristics of the target components.

The development of layer-by-layer GO membranes for the ion separation have been explored experimentally and numerically. Higher rejections of $Mg^{2+}$ and $Ca^{2+}$ could be experimentally achieved by surface charging because of the relatively stronger electrostatic repulsion by the membrane charge on the divalent ions than on the monovalent ions [12–15]. Such electrostatic repulsion is not capable of separating $Li^+$ from $Na^+$ or $K^+$. Instead, adsorption and size exclusion are two main mechanisms used for GO membrane design. Only a small number of experimental reports are available in the literature indicates the critical of channel size controlling [6,16–19]. Therefore, simulation work posed to be an alternative to provide a basis to design a high $Li^+$ selectivity membrane that could be synthesized in the future.

The difference in monovalent ion hydration shells is the basic separation mechanism used for simulation design. This difference consists of the interaction between the water molecules of the hydration shells, and the interaction between the water molecules and ions. As a case in point, talking $Li^+$, $Na^+$, and $K^+$ as a comparison basis for $Li^+$ separation, the dehydration energy of one water molecule follows the trend of hydrated $Li^+$> hydrated $Na^+$> hydrated $K^+$, while the hydration radius follows the trend of hydrated $Li^+$< hydrated $Na^+$< hydrated $K^+$ [20–26]. More energy is required when the ions need to dehydrate more that would result in lower ion permeance and better rejection. Summarized from the simulation works of porous GO membranes, pore size [27–31], and edge functionalization [30–33]have been reported as two dominant parameters that contribute to the separation of monovalent ions. Although the layer-by-layer GO membrane is easier to be prepared on a large scale, the numerical investigation on their monovalent ion separation performance is very limited. The effects of the edge functional groups on ion selectivity in a structure layer-by-layer GO membrane, which had significant impacts on the porous membrane, have never been examined before. Therefore, the effects of edge functional groups of the layer-by-layer GO membrane on the ion selectivity will be pursued in this current works.

To fill the gap in knowledge and find a strategy for selecting out $Li^+$ from other monovalent cations, i.e. $Na^+$ and $K^+$, layer-by-layer GO membranes, whose nanosheets were only edge functionalized by COOH, OH, and H respectively, were studied in this work. LiCl, NaCl, and KCl were separately processed for investigation with enhanced membrane edge effects. Membrane rejection performance and ion accumulation were analysed for identifying the influence of edge functionalization on the ion separation. In addition, a novel influence caused by the interaction between the compressed hydrated counter ions was also discussed to elucidate the ion entering competition at the long narrow functionalized entrance. This analysis expands the boundary of cation only analysis, which could undoubtedly simplify and highlight the key differences in separation but neglects any possible of the anions in affecting the separation process [27–29]. To the best of our knowledge, this part has never been discussed in other work.

## 2. Methodology

Four simulation models were used in this work that included equilibrium and non-equilibrium simulations ran by the large-scale atomic/molecular massively parallel simulator (LAMMPS) [34]. The overall membrane performance, the interaction between hydrated ions in bulk water, inside the interlayer channels, and under the influence of different edge functional groups were separately illustrated. Models were all solvated by the simple point charge (SPC) water molecules that applied with the SHAKE algorithm [35,36]. A time step of 2 fs and a temperature of 300 K were chosen for simulation. The Lennard-Jones (LJ) potential was cut-off at 9 Å and mixed with the Lorentz-Berthelot mixing roles (Table A1) [22,24,37–40]. Kspce_style Particle-Particle and Particle-Mesh Method (PPPM) solver was used for calculating the long-range electrostatic interaction. All simulation system was extended by the periodic boundary condition in all axis. This extension in the x and y-axis enlarged the membrane while the boundary in the z-axis was set far away from the membrane to keep the system in equilibrium.

### 2.1. Nanosheet structures

All-atom GO nanosheet models were built and charged through VEGA_ZZ 3.11 [41,42]. Three typical edge functional groups – COOH, OH, and H that are possible to be at the edge of nanosheet according to reported experimental observation-were individually linked at all edge carbons of the graphite nanosheets [43,44]. The orientation of the edge functional groups was randomly set. No surface functional group was utilized for simplifying the model. Functionalized nanosheets were relaxed to achieve its natural configurations corresponding to the numerical parameters used.

### 2.2. Filtration system for separating ions from water molecules

Based on the simulation results of our previous work, membrane structure that has a narrow interlayer channel (space size was determined by the distance between two carbon atoms from two adjacent layers of the membrane) and wide hub space (space size was determined by the distance between two closest atoms from two adjacent nanosheets in the same layer of the membrane) could achieve decent separation performance in a balance of high ion selectivity and high water permeance [45]. This type of membrane structure was used here to study the edge effect of GO nanosheet on different ions (Fig. 1a) by duplicating the edge functionalized nanosheets (size at around 28 × 44 $Å^2$) and placing them orderly as layer-by-layer membranes (Fig. 1a). The interlayer distance was 8 Å because the G-COOH membrane was not permeable to ions with 7 Å interlayer distance. Since the hub width was suggested to have very little influence on ions among different kinds of edges when the width was 7 Å and a wide hub space was more realistic than a narrow one, 12 Å hub width was used in this work for long interlayer channels and wide hub spaces [45]. Two impermeable nanosheets were placed on the top and the bottom of the system where were 60 Å and 20 Å away from the membrane, respectively (represented by the blue square in Fig. 1a, the bottom nanosheet is hidden in the figure for simplification). The boundary of the z-axis was set to be far away from the impermeable nanosheets. For simplifying the comparison of edge effects and accelerating the stabilizing process of filtration, the same concentration at 0.5 mol/L of LiCl, NaCl, KCl (around 190 ions were solvated by around 9850 water molecules as feed solution. Those numbers were slightly different when treated by different membranes), or pure water filled the space between the membrane and the top impermeable nanosheet. In the meantime, pure water molecules filled the membrane and the penetrant reservoir (around 3520 water molecules trapped by the membrane and the bottom impermeable nanosheet, numbers were slightly different when solvating different membranes).

System equilibrium was achieved by setting the membrane as fixed throughout the whole simulation. The movable impermeable nanosheets, water molecules, and ions were relaxed in the canonical ensemble (NVT) at 300 K with a time step at 2 fs for 0.5 ns to equilibrium the system. The hydraulic pressure used for the overall performance was mimicked by pushing the atoms of the top impermeable nanosheet downward along the z axis with a 3 kcal/(mol•Å) force every 10 steps. The atoms of the bottom impermeable nanosheet were pushed upward along the z axis with a 0.01 kcal/(mol•Å) force every 10 steps to keep the penetrant reservoir in equilibrium. The transmembrane pressure was 1091 MPa on the G-COOH membrane, 1028 MPa on the G-OH membrane, and 969.7 MPa on the G-H membrane when pure water was treated (Table A2). The pressure could be slightly different when different solutions were treated by the membrane because of the blockage of ions. The filtration processes stopped before running out of the feed solution, which was varied from 2.5 ns to 4.5 ns. The overall filtration performance of each solution and each membrane was repeated three times for obtaining the average value.

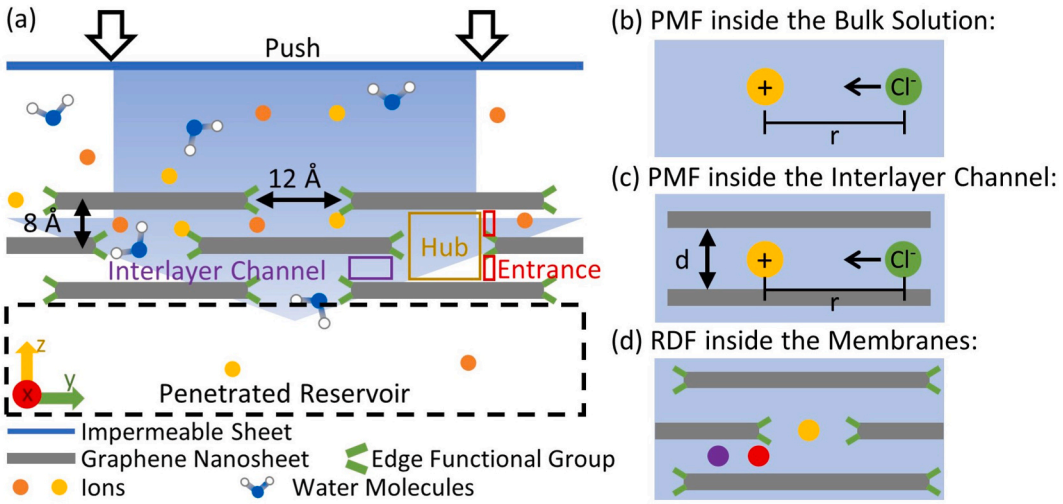


**Fig. 1.** Simulation models. (a) Filtration system for sieving ions out of water molecules. The location of an interlayer channel is represented by a purple rectangle, a hub space is illustrated as a yellow rectangle, and interlayer entrances are represented by red rectangles. (b–c) Models for calculating the PMF when ions are in (b) the bulk water or (c) inside interlayer channels whose d = 8 Å or d = 10 Å. (d) Model for simulating the RDF of the ion hydration shells inside the edge functionalized membranes. Locations include in the middle of hub space-yellow, at the interlayer entrance-red, and inside the interlayer channels-purple. (For interpretation of the references to colour in this figure legend, the reader is referred to the Web version of this article.)

The number of penetrant water molecules and ions was counted and plotted. The slope of number to time was defined as molecule permeance. Membrane selectivity was defined as the ratio of ion permeance to water permeance. The ion permeance ratio was defined as the ratio of two ion permeance that were separately treated by the same type of membrane. The ion concentration map showed the ion distribution inside the membranes on the yz surface. It was averaged from 100 ps. The entrance ion concentration maps and its permeance number maps were collected from the xz surface and averaged from the solution in thickness at 5 Å. They were collected over 1 ns from the G-COOH, G-OH, and G-H membranes, respectively. The membrane permeance number showed the number of same types of ions that had ever stopped at different locations at the entrances.

### 2.3. The potential of mean force (PMF)

When calculating the PMF, one cation was set fixed in the vicinity (surrounded) of water molecules (Fig. 1b) or in the middle of the interlayer channels with a width d of 8 or 10 Å (Fig. 1c). The 8 Å interlayer distance was meant for reproducing a similar degree of ion dehydration and hydration shell flattening in the membrane structure, while the 10 Å distance was meant for comparison. One $Cl^-$ was originally put 10 Å away from the target cation. Metadynamics simulation of a harmonic biasing method was ran in the isothermal-isobaric (NPT) ensemble at 1 atm with window width at 0.2 Å and moving restraints towards the cation at 1 Å/ns [46].

### 2.4. The ion radius of function (RDF) inside the membranes

The membrane was numerically immersed in the SPC water molecules. Depending on the cases, one $Li^+$, $Na^+$, $K^+$, and $Cl^-$ ions were then positioned inside the edge functionalized membranes, which included: in the middle of the hub, inside the interlayer channel, and at the entrance. Locations at the entrance were chosen according to the ion concentration. The simulation was run in NPT at 1 atm for 2 ns for calculating their RDFs with water molecules [47].

## 3. Results and discussions

### 3.1. Overall ion selectivity with different edge functional groups

LiCl, NaCl, and KCl were numerically treated by the G-COOH, G-OH, and G-H membranes to evaluate their selective performance, respectively. The G-COOH and G-H membranes had similar performance in

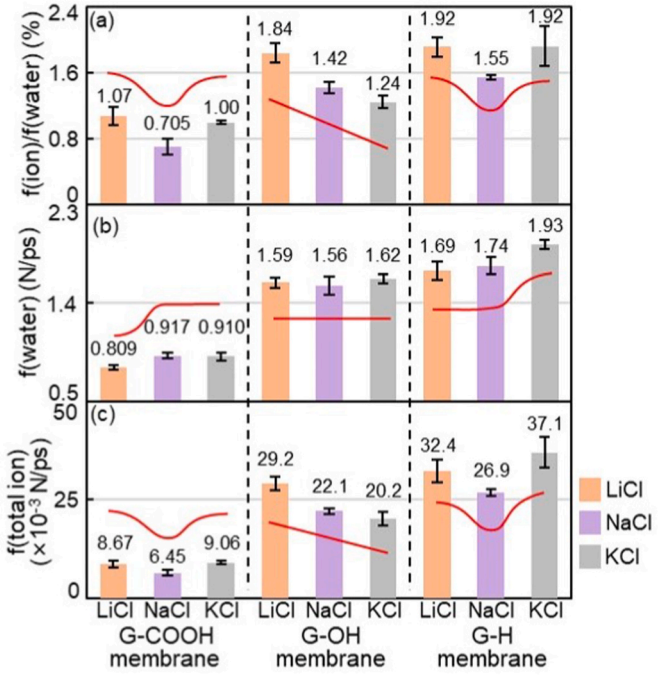


**Fig. 2.** Separation performances of membranes whose nanosheets were edge functionalized by the COOH, OH, and H. (a) Membrane selectivity of total ion to water, (b) water permeance, and (c) total ion permeance. Red lines highlight the difference between the three kinds of solutions. Membrane performances were calculated from the data plotted in Fig.A1. Separate selectivity f(cation)/f(water) and f(Cl-)/f(water) are shown in Fig. A2. (For interpretation of the references to colour in this figure legend, the reader is referred to the Web version of this article.)

which both had a relatively higher rejection of NaCl and higher permeance on LiCl and KCl (Fig. 2a). Although the G-COOH and G-H membranes had different water permeance characteristics (Fig. 2b, the former restricted water permeance when LiCl solution was treated, while the latter promoted the water permeance when KCl solution was treated), their trends of ion/water selectivity followed that of the absolute ion permeance (Fig. 2a and c). In contrast, the G-OH membrane showed different behaviour. Its ion permeance trend was LiCl > NaCl > KCl (Fig. 2c). Water permeance was not affected by the ion blockage at the OH entrance and therefore the ion/water selectivity followed the same trend as the total ion permeance. (Fig. 2a and c).

Based on this, it appeared that the G-COOH and G-H membranes can be used to separate out NaCl from other monovalent ions (at least the two ions evaluated here) by retaining NaCl in the retentate stream. In contrast, the G-OH membrane will be more suited to separate out LiCl from other ions by allowing selective permeance of LiCl. As alluded in the discussion so far, these ion separation characteristics are a combined effect of (1) the effect of ions on water permeance under different edge functional groups; and (2) the ion permeance under different edge functional groups. Although the ion separation characteristic is denoted by the ion/water permeance ratio, this inherent behaviour will be augmented by the water permeance rate. Therefore, in the following sections, we will attempt to elucidate the reason behind the trends observed for these two characteristics.

### 3.2. *Effects of edge functional groups and the type of monovalent ions on the water permeance*

As a basis for this discussion, the filtration of pure water was firstly taken as a reference. The water permeance takes the following trend of G-COOH < G-OH < G-H membranes (Fig. 3a). This trend corresponds to the difference in the effective entrance area (into the hub space of the membrane layers) as affected by the geometric size of the steric structure of the edge functional groups (Fig. 3b–e, for more discussion about the edge effects on water permeance, please see Refs. [38,45]).

The introduction of ions in the solution overall reduced the water permeance rate across the three types of edge functional membranes (Figs. 2b and 3a). This is due to the accumulation of the hydrated ions in the vicinity of the interlayer entrance (Fig. 3f–h, the red area in the contour plots show the locations of ion accumulation) which effectively limits the space available for free water transport. We will call this the hydrated ion blocking mechanism. Building upon this mechanism, the presence of ions further led to a few unique augmentations in the water permeance behaviour: (1) minimization of the difference in water permeance between the G-OH and G-H membranes despite the significant differences in their effective geometrical area for transport; (2) selective decrement of the water permeance across the G-COOH membrane in the presence of $Li^+$ ions; and (3) selective increment of the water permeance across the G-H membrane in the presence of $K^+$ ions.

In general, the G-H membrane exhibited a higher accumulation of ions (more space occupied) in the vicinity of the H entrance to the interlayer region when compared to the OH entrance (Fig. 3f and g). One can argue that inherently, the entrance space of the G-H membrane was larger due to the smaller steric structure of the H atom. If we compare the cross-section area occupied by the hydrated ions (represented by the geometrically available $Cl^-$ transport area in Fig. 4a and c) relative to the effective geometrically available area of water molecules (Fig. 3b), the G-H and G-OH membranes exhibited similar ratios of 43% and 42%,

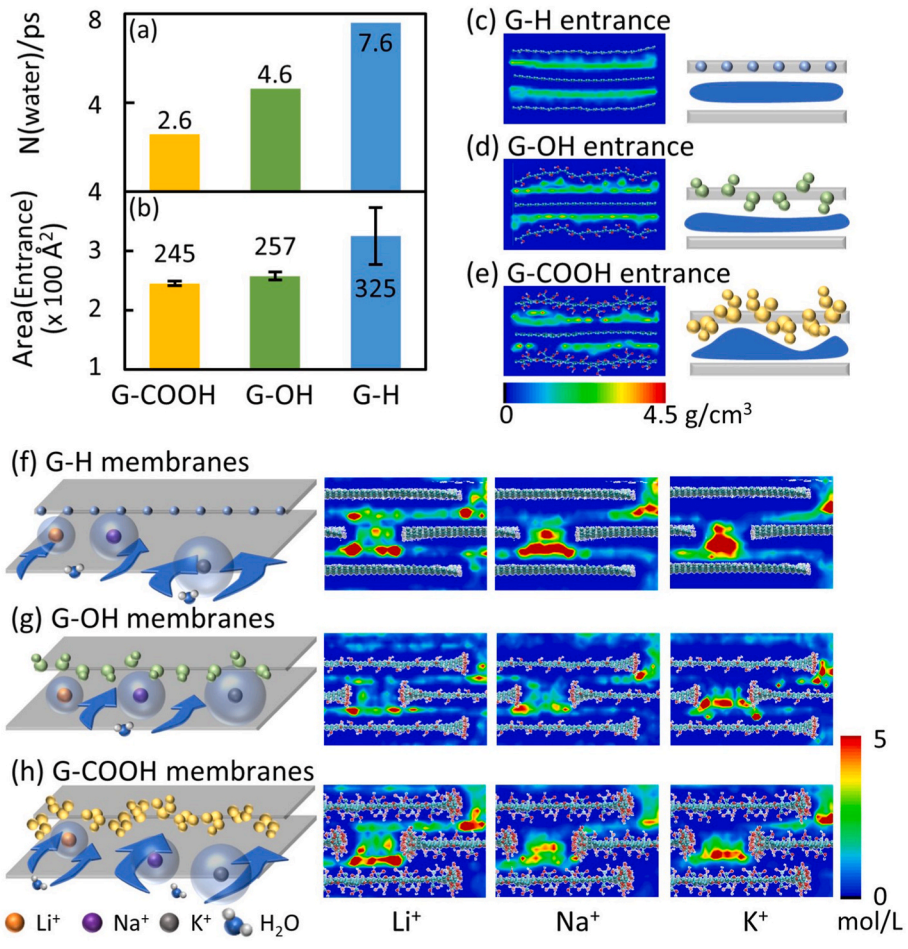


**Fig. 3.** (a) Water permeance of edge functionalized membranes when pure water was treated. (b) Effective entrance area for water molecules at the functionalized entrances. All effective water entrances are shown in Fig. A3. (c–e) Water concentration maps (represented by O atoms) at the entrances and their simplified illustrations. (f–h) Simplified ion blockage illustrations and ion concentration maps of the (f) G-H, (g) G-OH, and (h) G-COOH membranes. Full ion concentration maps are shown in Fig. A4.

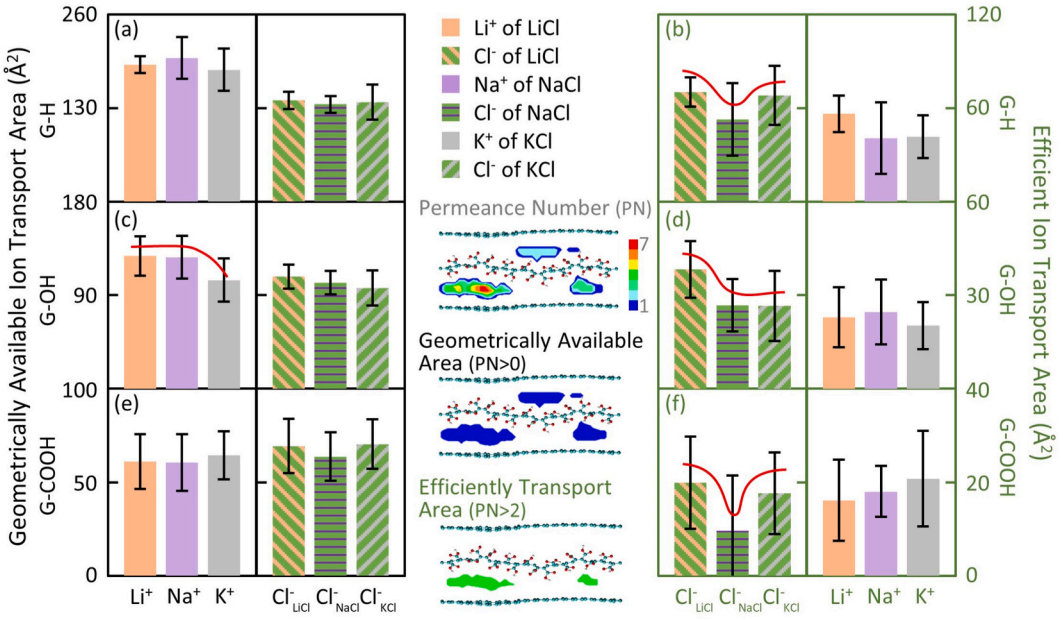


**Fig. 4.** (a, c, e) Geometrically available ion transport area where ions had ever stopped at the (a) G-H, (c) G-OH, and (e) G-COOH entrances (permeance number > 0 in Fig. A5). (b, d, f) Effective ion transport area where ions could effectively go through (permeance number > 2 in Fig. A5). Red lines highlight the difference between the three kinds of solutions. Permeation number and ion concentration at different entrances are shown in Fig. A5 and Fig. A6, respectively. (For interpretation of the references to colour in this figure legend, the reader is referred to the Web version of this article.)

respectively. Therefore, this expresses that the ion blocking mechanism effectively negated the differences in the inherent water permeance characteristics between the two edge functionalized membranes.

From examining the ion concentration map for the G-H membrane (Fig. 3f), the hydrophobic H edge did not attract ions by pulling their hydrated shells. Hence, the $K^+$ with larger hydrated size mainly accumulated within the central region of the hub space whereas the accumulation of the $Li^+$ and $Na^+$ with relatively smaller hydrated sizes stretched into the narrow entry region of the interlayer channel (Fig. 3f and Fig. A7). Therefore, in effect, the presence of $K^+$ led to relatively lesser hydrated ion blocking and higher water permeance.

The COOH groups of the G-COOH membrane, in a reversed manner,

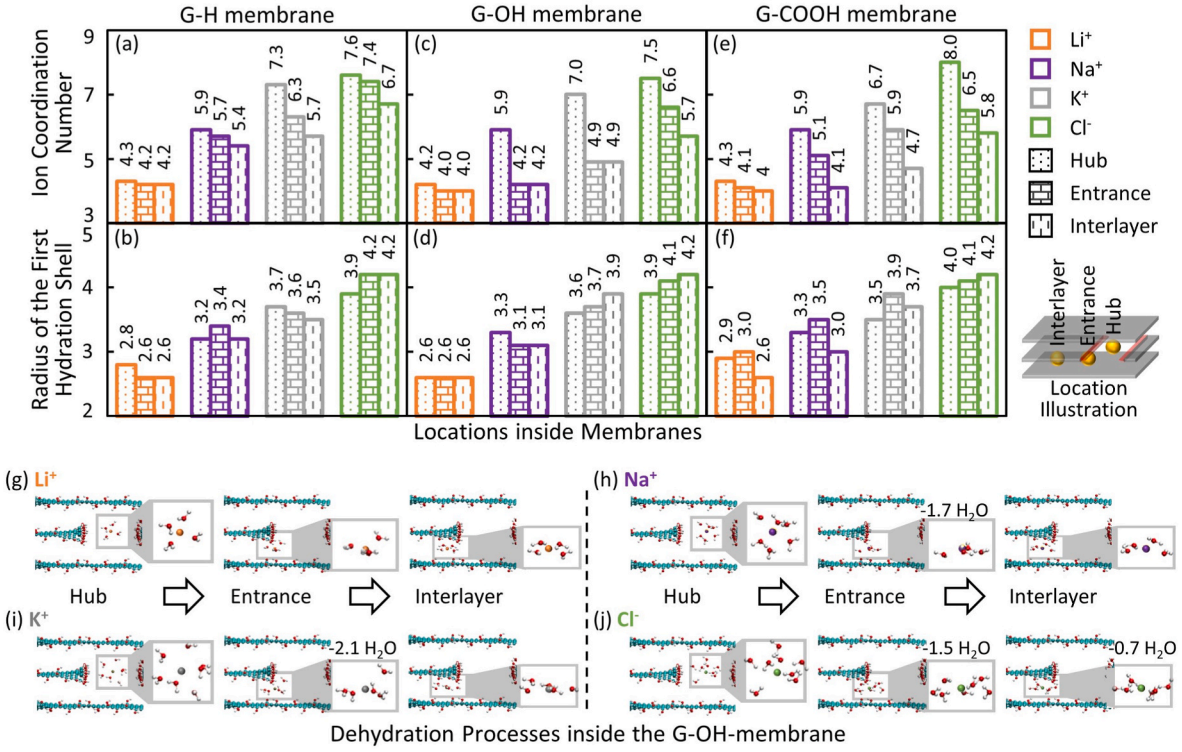


**Fig. 5.** Ion dehydration processes inside the edge functionalized membranes. (a, c, e) Ion coordination numbers and (b, d, f) radius of the first hydration shells when ions inside the (a–b) G-H, (c–d) G-OH, and (e–f) G-COOH membranes. (g–j) Screenshots of the hydrated ions inside the G-OH membrane. The screenshots of the hydrated ions inside the G-H and G-COOH membranes are shown in Fig. A8.

introduced significant tortuosity into the nanosheet configuration by their large geometric steric structure for ion transport (Fig. 3e). This hydrophilic edge consists of hydroxyl and carbonyl groups that could strongly attract ions by pulling their hydrated shells. The size of the hydrated $Li^+$ is smaller than $Na^+$ and $K^+$ (Fig. A7). This led to a higher accumulation of $Li^+$ and stronger hydrated ion blocking (Fig. 3h). Hence, selectively lower water permeance could be observed (Fig. 2b). Such selective accumulation of ions in the vicinity of the entrance of the interlayer channels was not observed inside the G-OH membrane because of its medium level in the geometric entrance size and hydrophilicity (Fig. 3g).

### 3.3. Effects of edge functional groups on the ion permeance

We will now attempt to elucidate how the different edge functional groups affected and resulted in the inherent ion selectivity trend shown in Fig. 2c. The specific trends are (1) the G-OH membrane shows a decreasing trend in ion permeance with $Li^+ > Na^+ > K^+$, and (2) the G-COOH and G-H membranes show similar permeance between $Li^+$ and $K^+$ but exhibit a selective dip in permeance of $Na^+$.

Ion dehydration is one main mechanism that has been widely reported to affect selective ion permeance [20,27,48]. Exploring this potential mechanism, ion coordination numbers, and radius of the respective hydration shells of the ions as they move from the hub space to the interlayer channel, are analysed (Fig. 5). Due to the small size of the hydrated $Li^+$ ion (Fig. A7 and Fig. A8), there was very minimal dehydration as it moves across the membrane structure for all three functionalized membranes evaluated. This explains the relatively higher ion permeance of $Li^+$ observed in the overall filtration processes (Fig. 2c).

Nevertheless, the hydrated $Na^+$ and $K^+$ ions experience significant dehydration and their respective dehydration behaviour was affected by the edge functional groups (Fig. 5). In the G-OH membrane, there was a sudden step of dehydration as the ions moved into the entrance of the interlayer channel. $Na^+$ averagely lost 1.7 water molecules while $K^+$ averagely lost 2.1 water molecules. As the ions moved through the interlayer channel, however, no more dehydration was detected (Fig. 5c). For the G-COOH and G-H membranes, such a drastic step of dehydration was not observed. It was replaced with a progressive two-step dehydration behaviour and each step of them lost averagely less than 1.2 water molecules (Fig. 5a and e).

Based on this observation, when moving across the G-OH membrane, the hydrated $Na^+$ and $K^+$ experienced relatively more significant energy barrier resistance when compared to the hydrated $Li^+$. It resulted in significantly lower $Na^+$ and $K^+$ permeance than $Li^+$ (Fig. 2c). Such an energy barrier mechanism has also been widely reported by other works as a key mechanism for ion permeance selectivity [20,27,48]. For the G-COOH and the G-H membrane, however, the energy barrier resistance could not explain the selectivity trend observed: within the range of fluctuations observed, $Li^+$ and $K^+$ have similar permeance values while there was a significant dip in permeance for the $Na^+$. Building on top of the dehydration mechanism discussed, there may be two possibilities leading to this discrepancy: either (1) the progressive two-step dehydration did not result in significant energy barrier relative to the high pressure 'pushing' environment, or (2) there was any additional mechanism at play leading to a decrease in the permeance of $Na^+$. The former possibility which negates the possible contribution of dehydration energy barrier on ion selectivity also implies that there is an additional mechanism leading to the significant dip in $Na^+$ permeance.

To ascertain these two possibilities, we further examined another characteristic observed on the ion hydration shell: its shape was compressed and deviated from a spherical structure into a ring shape at the narrow interlayer channel (Fig. 5g–j). For the evaluation purpose, we reproduced the dehydrated ion hydration shells with simplified models that compressed the hydrated ions through two graphite nanosheets (Fig. 1b and c). When the interlayer distance was set at 10 Å, water molecules surrounding the ions were of a semi-spherical doughnut shape (Fig. 6a–d). The ions did not experience dehydration, but their coordination numbers were slightly increased by the high-water density on the surface of the graphite nanosheets (Fig. 6e). When the interlayer distance was decreased to 8 Å that was the same as the edge functionalized membranes, the water molecules surrounding the cations formed a ring structure. The volumes of the hydrated shells were about half as before, but their radius was barely changed while the coordination numbers were only slightly reduced. The water densities of the compressed hydrated shells were therefore increased (Fig. 6). A similar high-density hydration shell could also be obtained when ions were inside the functionalized membranes (Fig. 5).

Looking from the top view of the ring-shape hydration shells, water molecules showed a clear orientation around the ions (Fig. 6a–d). The negatively charged oxygen atoms of the water molecules pointed towards the cations while the positively charged hydrogen atoms of the water molecules pointed towards the $Cl^-$. Because of their larger sizes in volume than ions, those flattened high-density hydration shells enhanced the influence of surroundings on the ions. Especially, they also tuned the effects between the vicinity counter ions that had similar 'hydrated jackets' which were affected by variety of dehydration degrees at different locations inside the functionalized membranes.

PMF analysis of an approaching $Cl^-$ inside the graphite interlayer channel help to study the effect of the flattened hydration shell with structured water molecules on the cation-anion interaction. In the unrestricted non-compressed condition, as a $Cl^-$ approaches a $Li^+$, the anion will be slightly attracted between 3.5 and 4.5 Å followed by repulsion at about 3.0 Å (Fig. 6g). Nevertheless, the compressed hydration shell 'pushed' the repulsion region further out to about 3.8 Å. In the meantime, it enhanced the attraction delineated by the significantly lower energy between 3.8 and 4.5 Å. This unique attraction region may promote $Cl^-$ permeance, which will further enhance the $Li^+$ and therefore increase the overall LiCl permeance through the electrostatic interaction caused by the asymmetric ion distribution across the functionalized membranes (Fig. 2 and Fig. A1). The phenomenon of the electrostatic interaction caused by the asymmetric ion distribution across the functionalized membranes please refer [45].

Similar $Cl^-$ repulsion regions caused by the hydration shells of the $Na^+$ and $K^+$ were also observed (Fig. 6g). Under the compression at the 8 Å interlayer channel, the enhancement of the repulsion region was more significant for $Na^+$ than $K^+$, which was delineated by the higher energy barrier (Fig. 6g). This higher energy barrier caused by the compressed dehydrated hydration shell around the $Na^+$ makes the hydrated $Cl^-$ harder to approach, which will further reduce the $Na^+$ and therefore decrease the overall NaCl permeance through the electrostatic interaction caused by the asymmetric ion distribution across the functionalized membranes (Fig. 2).

The effects between the hydrated cations and $Cl^-$ summarized from the simplified models through the ion movability at the functionalized entrance were visualized. According to the value of permeance number (the number of same types of different ions), the functionalized entrances were calculated and compared as geometrically available ion transport areas and efficiently ion transport areas (Fig. 4). The geometrically available ion transport area includes all locations where ions had ever been. Its permeance number was larger than 0, which means the ions' dehydration energy at that location could be overcome by the current hydraulic pressure. The efficient ion transport area is part of the geometrically available ion transport area. It includes all locations where the permeance number was larger than 2. This area was sensitively affected by the vicinity counter ions because it exhibited the locations of high ion permeance when they were surrounded by counter ions, which were attracted by their electrostatic interaction, and competing to enter the tiny functionalized entrance.

The geometrically available $K^+$ transport area was lower than the other cations at the OH entrance (Fig. 4c). Because it requires higher energy to achieve the drastic dehydration at the OH entrance, the area it

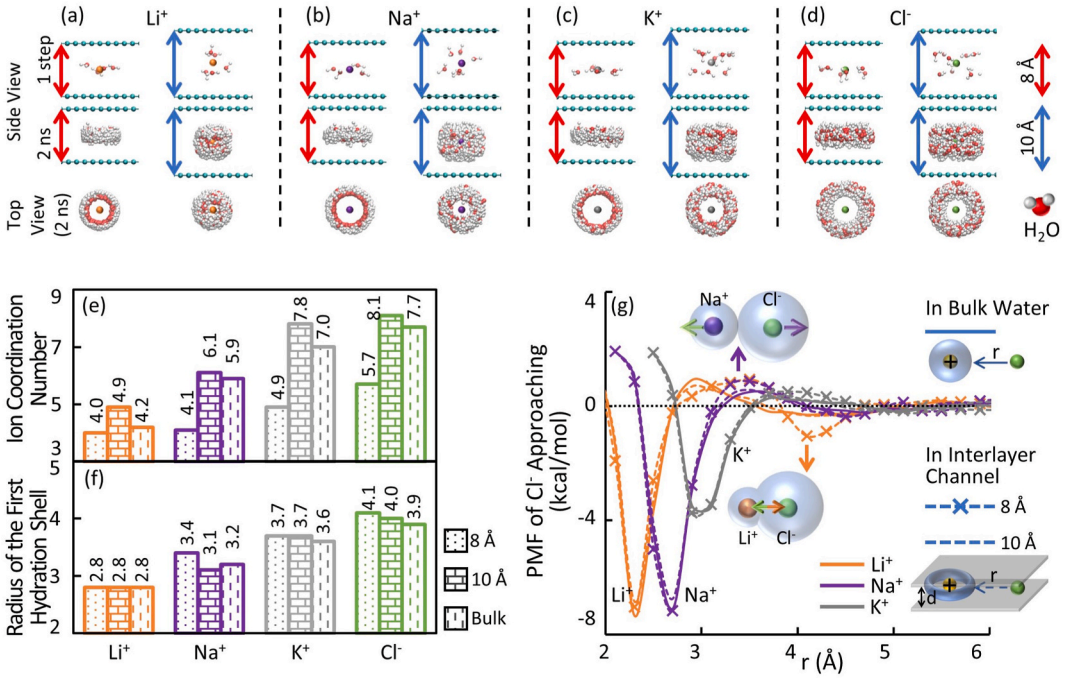


**Fig. 6.** (a–d) Screenshots of hydrated ions of 1 step and collected trajectories of every 2 ps for 2 ns. (e) Ion coordination numbers and (f) radius of the first hydration shells in the bulk, 8 Å and 10 Å interlayer channels. (g) PMF when a $Cl^-$ was pulled towards to a cation when they were in the bulk water (represented by the solid lines) or inside the interlayer channels whose d = 8 Å (represented by the crossed dash lines) or d = 10 Å (represented by the dash lines). RDFs between ions and water molecules in the bulk or inside the interlayer channels are shown in Fig. A9.

could reach under the current hydraulic pressure was limited. Therefore, the G-OH membrane had lower KCl permeance (Fig. 2c). Similar decrement in the geometrically available Na + transport area at the OH entrance was not observed for fewer water molecules it dehydrated (Figs. 4c and 5c).

At the G-H and G-COOH entrances, $Na^+$ and $K^+$ progressively dehydrated (Fig. 5a and e). H edge was the smallest functional group leading to the largest entrance area (Fig. 3b). It allowed more water molecules to be positioned in the vicinity adjacent to the ions. Thus, the hydrated ions could lose water progressively at the H entrance. The OH and COOH edges were larger than the H edge that reduced the entrance area (Fig. 3b). Nanosheets were twisted when they were edge functionalized by the OH or COOH functional groups (Fig. 3c–e). Because of the repulsion and larger size of the COOH functional groups, the COOH entrance was significantly enlarged at some locations by the tortuosity introduced by the COOH functional groups. This enlargement was less by the OH for smaller volumetric size, which meant that a higher degree of dehydration is required for the passing of the ion. Consequently, the hydrophilic of the G-COOH was incapable of forcing a sudden step of dehydration, and progressive dehydration was only observed inside the G-H and G-COOH membranes (Fig. 3c and e). This two-step dehydration process did not require high dehydration energy and could be easily overcome by the hydraulic pressure. Therefore, they had similar geometrically available ion transport areas as $Li^+$, which was barely dehydrated at the entrances (Fig. 4a and e).

The geometrically available $Cl^-$ transport area was the same when different solutions were processed by same type of membranes (Fig. 4a, c, and e). Nevertheless, the efficient $Cl^-$ transport area, which was sensitively affected by the environments, was changed when different cations presented vicinity (Fig. 4b, d, and f). Inside the G-COOH and G-H membranes, the efficiently $Cl^-$ transport area was reduced when the NaCl solution was treated (Fig. 4b and f). This decrease exhibited the repulsion caused by their compressed hydration shells (Fig. 6g). Inside the G-OH membrane, the efficiently $Cl^-$ transport was improved when the LiCl was treated. This increase showing the attraction between the hydrated $Li^+$ and the hydrated $Cl^-$ at the long narrow OH entrance (Figs. 4d and 6g). More evidence supporting this attraction can be observed from the higher $Cl^-$ concentrate on inside the G-OH and G-COOH interlayer channels when $Li^+$ was presented (Fig. A4). Those additional attraction and repulsion acted by the hydrated cations on the $Cl^-$ could promote and reduce the $Cl^-$ permeance, respectively, which would further promote and reduce the cation and therefore influence the overall ion permeance by the electrostatic interaction caused by the asymmetric charge distribution of the draw and penetrant reservoirs [45].

Because of the complex configuration of the functionalized entrances, the geometrically available ion transport area and the effective ion transport area may not fully explain all trends. This visualized evidence, however, could directly support our discussion on the differences in the drastic and the progressive dehydration energy, as well as the interaction tuned by the compressed hydrated shells under the influence of edge functional groups.

## 4. Conclusion

In this work, the effects of three typical edge functional groups – COOH, OH, and H are compared on the layer-by-layer edge functionalized membranes selectivity when separately treating the LiCl, NaCl, and KCl solutions. A figure summarized the contribution of the three kinds of edge functional groups is shown in Fig. 7. The entrances of membrane interlayer channels are the main rejection location. The water permeance is dominantly determined by the steric size of the edge functional groups whereas it could be changed by the blockage of different ions at the interlayer entrance. The two-step progressive ion dehydration requires less dehydration energy than the drastic dehydration. The repulsion of the hydrated $Na^+$ on the hydrated $Cl^-$ reduces the overall permeance of NaCl ion and results in higher NaCl rejections of the G-COOH and G-H membranes (Fig. 7a and c). The drastic dehydration of $K^+$ and $Na^+$ results in lower KCl and NaCl permeance of the G-OH membrane. Meanwhile, the attraction of the hydrated $Li^+$ on the hydrated $Cl^-$ promotes the LiCl permeance of the G-OH membrane. Therefore, the G-OH membrane shows higher LiCl permeance than other

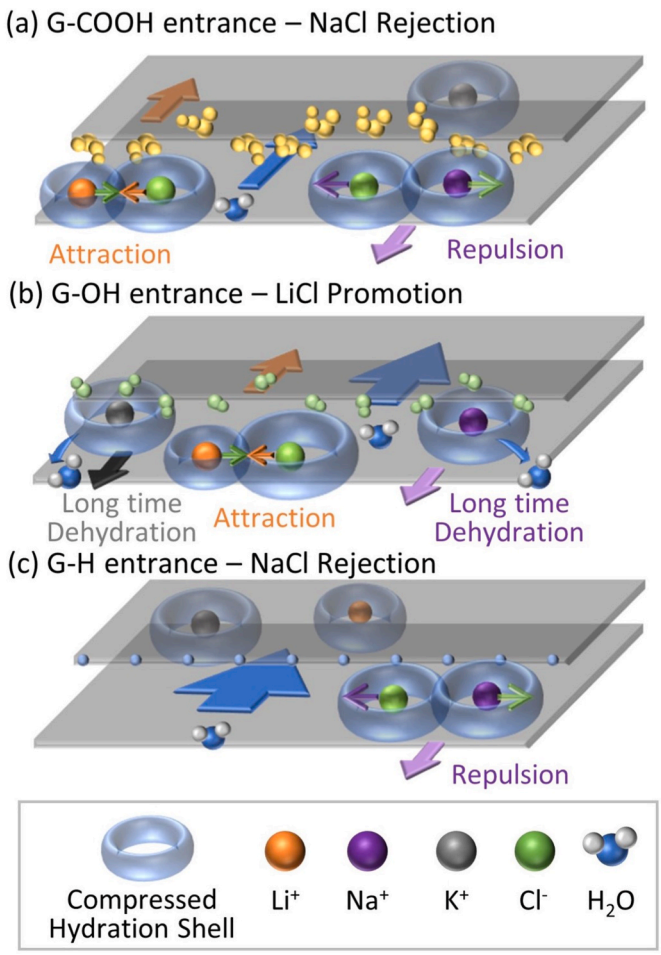


**Fig. 7.** Summarized ion rejection mechanism at the entrances of layer-by-layer membranes, which were functionalized by the (a) COOH edge, (b) OH edge, and (c) H edge.

solutions (Fig. 7b). Consequently, all kinds of functionalized edges have the potential to permeate LiCl by rejecting NaCl, while the OH edge might help to reject KCl additionally. A strategy summarized from this work is beneficial for future development: the COOH, OH, and H edges have the potential in sieving $Li^+$ out of $Na^+$ while OH edge is more recommended when the solution has high $K^+$ concentration.

## Author contributions

**Ruosang Qiu:** Data curation; Formal analysis; Investigation; Methodology; Validation; Visualization; Writing - original draft.

**Jie Xiao:** Funding acquisition; Writing - review & editing.

**Xiao Dong Chen:** Funding acquisition; Writing - review & editing.

**Cordelia Selomulya:** Funding acquisition; Writing - review & editing.

**Xiwang Zhang:** Funding acquisition; Conceptualization; Supervision; Writing - original draft.

**Meng Wai Woo:** Funding acquisition; Conceptualization; Supervision; Writing - original draft; Project administration.

## Declaration of competing interest

The authors declare that they have no known competing financial interests or personal relationships that could have appeared to influence the work reported in this paper.

## Acknowledgement

This project was supported by the Australian Government Department of Industry, Innovation, and Science through the Australia-China Science and Research Fund (ACSRF48154) and is conducted as a part of the research program of the Australia-China Joint Research Centre in Future Dairy Manufacturing (http://acjrc.eng.monash.edu/). Soochow University acknowledges The National Key Research and Development Program of China (International S&T Cooperation Program, ISTCP, 2016YFE0101200) for the support of the Australia-China collaboration.

## Appendix A. Supplementary data

Supplementary data to this article can be found online at https://doi.org/10.1016/j.memsci.2020.118892.

## References

[1] P.W. Gruber, P.A. Medina, G.A. Keoleian, S.E. Kesler, M.P. Everson, T. J. Wallington, Global lithium availability, J. Ind. Ecol. 15 (2011) 760–775, https://doi.org/10.1111/j.1530-9290.2011.00359.x.
[2] A. Panagopoulos, K.J. Haralambous, M. Loizidou, Desalination brine disposal methods and treatment technologies - a review, Science of the Total Environment, 2019, p. 693, https://doi.org/10.1016/j.scitotenv.2019.07.351.
[3] B. Swain, Recovery and recycling of lithium: a review, Separ. Purif. Technol. 172 (2017) 388–403, https://doi.org/10.1016/j.seppur.2016.08.031.
[4] C. Jiang, Y. Wang, Q. Wang, H. Feng, T. Xu, Production of lithium hydroxide from lake brines through electro–electrodialysis with bipolar membranes (EEDBM), Ind. Eng. Chem. Res. 53 (2014) 6103–6112, https://doi.org/10.1021/ie404334s.
[5] X. Li, C. Zhang, S. Zhang, J. Li, B. He, Z. Cui, Preparation and characterization of positively charged polyamide composite nanofiltration hollow fiber membrane for lithium and magnesium separation, Desalination 369 (2015) 26–36, https://doi.org/10.1016/j.desal.2015.04.027.
[6] R. Epsztein, E. Shaulsky, M. Qin, M. Elimelech, Activation behavior for ion permeation in ion-exchange membranes: role of ion dehydration in selective transport, J. Membr. Sci. 580 (2019) 316–326, https://doi.org/10.1016/j.memsci.2019.02.009.
[7] S. Kim, H. Wang, Y.M. Lee, 2D nanosheets and their composite membranes for water, gas, and ion separation, Angew. Chem. Int. Ed. 58 (2019) 17512–17527, https://doi.org/10.1002/anie.201814349.
[8] Y. Li, S. Yuan, Y. Xia, W. Zhao, C.D. Easton, C. Selomulya, X. Zhang, Mild annealing reduced graphene oxide membrane for nanofiltration, J. Membr. Sci. 601 (2020), https://doi.org/10.1016/j.memsci.2020.117900.
[9] Y. Li, W. Zhao, M. Weyland, S. Yuan, Y. Xia, H. Liu, M. Jian, J. Yang, C.D. Easton, C. Selomulya, X. Zhang, Thermally reduced nanoporous graphene oxide membrane for desalination, Environ. Sci. Technol. 53 (2019) 8314–8323, https://doi.org/10.1021/acs.est.9b01914.
[10] Y. Kang, Y. Xia, H. Wang, X. Zhang, 2D laminar membranes for selective water and ion transport, Adv. Funct. Mater. 29 (2019) 1902014, https://doi.org/10.1002/adfm.201902014.
[11] R.R. Nair, H.A. Wu, P.N. Jayaram, I.V. Grigorieva, A.K. Geim, Unimpeded permeation of water through helium-leak-tight graphene-based membranes. (REPORTS)(Author abstract)(Report), Science 335 (2012) 442, https://doi.org/10.1126/science.1211694.
[12] M. Zhang, K. Guan, Y. Ji, G. Liu, W. Jin, N. Xu, Controllable ion transport by surface-charged graphene oxide membrane, Nat. Commun. 10 (2019) 1253, https://doi.org/10.1038/s41467-019-09286-8.
[13] Y. Liu, S. Zheng, P. Gu, A.J. Ng, M. Wang, Y. Wei, J.J. Urban, B. Mi, Graphene-polyelectrolyte multilayer membranes with tunable structure and internal charge, Carbon 160 (2020) 219–227, https://doi.org/10.1016/j.carbon.2019.12.092.
[14] M. Caglar, I. Silkina, B.T. Brown, A.L. Thorneywork, O.J. Burton, V. Babenko, S. M. Gilbert, A. Zettl, S. Hofmann, U.F. Keyser, Tunable anion-selective transport through monolayer graphene and hexagonal boron nitride, ACS Nano 14 (2020) 2729, https://doi.org/10.1021/acsnano.9b08168.
[15] Y. Han, Z. Xu, C. Gao, Ultrathin graphene nanofiltration membrane for water purification, Adv. Funct. Mater. 23 (2013) 3693–3700, https://doi.org/10.1002/adfm.201202601.
[16] J. Shi, W. Wu, Y. Xia, Z. Li, W. Li, Confined interfacial polymerization of polyamide-graphene oxide composite membranes for water desalination, Desalination 441 (2018) 77–86, https://doi.org/10.1016/j.desal.2018.04.030.
[17] Y. Zhao, W. Shi, B. Van Der Bruggen, C. Gao, J. Shen, Tunable nanoscale interlayer of graphene with symmetrical polyelectrolyte multilayer architecture for lithium extraction, Adv. Mater. Interfaces 5 (2018) 1701449, https://doi.org/10.1002/admi.201701449.
[18] Z. Zhao, S. Ni, X. Su, Y. Gao, X. Sun, Thermally reduced graphene oxide membrane with ultrahigh rejection of metal ions' separation from water, ACS Sustain. Chem. Eng. 7 (2019) 14874–14882, https://doi.org/10.1021/acssuschemeng.9b02972.
[19] X. Li, B. Zhu, J. Zhu, Graphene oxide based materials for desalination, Carbon 146 (2019) 320–328, https://doi.org/10.1016/j.carbon.2019.02.007.

[20] Y. Fu, S. Su, N. Zhang, Y. Wang, X. Guo, J. Xue, Dehydration-determined ion selectivity of graphene subnanopores, ACS Appl. Mater. Interfaces 12 (2020), https://doi.org/10.1021/acsami.0c03932.
[21] S.H. Lee, J.C. Rasaiah, Molecular dynamics simulation of ion mobility. 2. Alkali metal and halide ions using the SPC/E model for water at 25 °C, J. Phys. Chem. 100 (1996) 1420–1425, https://doi.org/10.1021/jp953050c.
[22] H. Yan, S.L. Yuan, G.Y. Xu, C.B. Liu, Effect of Ca2+ and Mg2+ ions on surfactant solutions investigated by molecular dynamics simulation, Langmuir 26 (2010) 10448–10459, https://doi.org/10.1021/la100310w.
[23] A.P. Lyubartsev, A. Laaksonen, Concentration effects in aqueous NaCl solutions. A molecular dynamics simulation, J. Phys. Chem. 100 (1996) 16410–16418, https://doi.org/10.1021/jp961317h.
[24] S. Bouazizi, S. Nasr, Local order in aqueous lithium chloride solutions as studied by X-ray scattering and molecular dynamics simulations, J. Mol. Struct. 837 (2007) 206–213, https://doi.org/10.1016/j.molstruc.2006.10.017.
[25] Z. Zhang, Z. Duan, Lithium chloride ionic association in dilute aqueous solution: a constrained molecular dynamics study, Chem. Phys. 297 (2004) 221–233, https://doi.org/10.1016/j.chemphys.2003.10.030.
[26] S. Chowdhuri, A. Chandra, Molecular dynamics simulations of aqueous NaCl and KCl solutions: effects of ion concentration on the single-particle, pair, and collective dynamical properties of ions and water molecules, J. Chem. Phys. 115 (2001) 3732–3741, https://doi.org/10.1063/1.1387447.
[27] N. Zhao, J. Deng, Y. Zhu, Y. Chen, Y. Qin, Y. Ruan, Y. Zhang, Q. Gao, X. Lu, Atomistic insights into the effects of carbonyl oxygens in functionalized graphene nanopores on Ca2+/Na+ sieving, Carbon 164 (2020) 305–316, https://doi.org/10.1016/j.carbon.2020.04.018.
[28] Y. Liu, D. Xie, M. Song, L. Jiang, G. Fu, L. Liu, J. Li, Water desalination across multilayer graphitic carbon nitride membrane: insights from non-equilibrium molecular dynamics simulations, Carbon 140 (2018) 131–138, https://doi.org/10.1016/j.carbon.2018.08.043.
[29] A. Fang, K. Kroenlein, D. Riccardi, A. Smolyanitsky, Highly mechanosensitive ion channels from graphene-embedded crown ethers, Nat. Mater. 18 (2019) 76, https://doi.org/10.1038/s41563-018-0220-4.
[30] Y. Wang, Z. He, K.M. Gupta, Q. Shi, R. Lu, Molecular dynamics study on water desalination through functionalized nanoporous graphene, Carbon 116 (2017) 120–127, https://doi.org/10.1016/j.carbon.2017.01.099.
[31] D. Konatham, J. Yu, T.A. Ho, A. Striolo, Simulation insights for graphene-based water desalination membranes, Langmuir 29 (2013) 11884–11897, https://doi.org/10.1021/la4018695.
[32] C. Fang, Z. Yu, R. Qiao, Impact of surface ionization on water transport and salt leakage through graphene oxide membranes, J. Phys. Chem. C 121 (2017) 13412–13420, https://doi.org/10.1021/acs.jpcc.7b04283.
[33] Y. Li, Z. Xu, S. Liu, J. Zhang, X. Yang, Molecular simulation of reverse osmosis for heavy metal ions using functionalized nanoporous graphenes, Comput. Mater. Sci. 139 (2017) 65–74, https://doi.org/10.1016/j.commatsci.2017.07.032.
[34] S. Plimpton, Fast parallel algorithms for short-range molecular dynamics, J. Comput. Phys. 117 (1995) 1–19, https://doi.org/10.1006/jcph.1995.1039.
[35] W.L. Jorgensen, J. Chandrasekhar, J.D. Madura, R.W. Impey, M.L. Klein, Comparison of simple potential functions for simulating liquid water, J. Chem. Phys. 79 (1983) 926–935, https://doi.org/10.1063/1.445869.
[36] P. Mark, L. Nilsson, Structure and dynamics of the TIP3P, SPC, and SPC/E water models at 298 K, J. Phys. Chem. 105 (2001) 9954–9960.
[37] D. Boda, D. Henderson, The effects of deviations from Lorentz-Berthelot rules on the properties of a simple mixture, Mol. Phys. 106 (2008) 2367–2370, https://doi.org/10.1080/00268970802471137.
[38] R. Qiu, S. Yuan, J. Xiao, X.D. Chen, C. Selomulya, X. Zhang, M.W. Woo, Effects of edge functional groups on water transport in graphene oxide membranes, ACS Appl. Mater. Interfaces 11 (2019) 8483–8491, https://doi.org/10.1021/acsami.9b00492.
[39] B. Chen, H. Jiang, X. Liu, X. Hu, Molecular insight into water desalination across multilayer graphene oxide membranes, ACS Appl. Mater. Interfaces 9 (2017) 22826–22836, https://doi.org/10.1021/acsami.7b05307.
[40] W.L. Jorgensen, D.S. Maxwell, J. Tirado-Rives, Development and testing of the OPLS All-Atom force field on conformational energetics and properties of organic liquids, J. Am. Chem. Soc. 118 (1996) 11225–11236, https://doi.org/10.1021/ja9621760.
[41] J. Gasteiger, M. Marsili, Iterative partial equalization of orbital electronegativity-a rapid access to atomic charges, Tetrahedron 36 (1980) 3219–3228, https://doi.org/10.1016/0040-4020(80)80168-2.
[42] M. Marsili, J. Gasteiger, Pi-charge distribution from molecular topology and pi-orbital electronegativity, Croat. Chem. Acta 53 (1980) 601–614.
[43] A. Lerf, H. He, M. Forster, J. Klinowski, Structure of graphite oxide revisited, J. Phys. Chem. B 102 (1998) 4477–4482.
[44] D.R. Dreyer, S. Park, C.W. Bielawski, R.S. Ruoff, The chemistry of graphene oxide, Chem. Soc. Rev. 39 (2009) 228–240, https://doi.org/10.1039/b917103g.
[45] R. Qiu, J. Xiao, X.D. Chen, C. Selomulya, X. Zhang, M.W. Woo, Relationship between desalination performance of graphene oxide membranes and edge functional groups, ACS Appl. Mater. Interfaces 12 (2020), https://doi.org/10.1021/acsami.9b19976.
[46] G. Fiorin, M.L. Klein, J. Hénin, Using collective variables to drive molecular dynamics simulations, Mol. Phys. 111 (2013) 3345–3362, https://doi.org/10.1080/00268976.2013.813594. Special Issue in Honour of Giovanni Ciccotti on the Occasion of his 70th Birthday.
[47] D. Frenkel, B. Smit, M.A. Ratner, Understanding molecular simulation: from algorithms to applications, Phys. Today 50 (1997), https://doi.org/10.1063/1.881812, 66-66.
[48] Q. Liu, Y. Liu, G. Liu, Simulation of cations separation through charged porous graphene membrane, Chem. Phys. Lett. (2020) 753, https://doi.org/10.1016/j.cplett.2020.137606.